COMPARISON OF BEHAVIOUR OF BURNT BEAMS MODELS WITH EFFECTIVE AND ACTUAL RESIDUAL CROSS-SECTIONS IN THREE POINT BENDING TEST

LUCIE KEŘKOVÁ KUCÍKOVÁ*, MICHAL ŠEJNOHA, TOMÁŠ JANDA, PAVEL PADEVĚT

Czech Technical University in Prague, Faculty of Civil Engineering, Department of Mechanics, Thákurova 7, 166 29 Prague 6, Czech Republic

* corresponding author: `lucie.kucikova@fsv.cvut.cz`

ABSTRACT. Glued laminated timber beams exposed to fire of a variable duration were tested in three point bending. Three types of model geometries taking into account the effect of burning were created. Each model was examined for five material data sets. The maximum deflection obtained from FEM simulations was compared with the corresponding deflection w_{el} derived from a three point bending test of burnt beams. The analysis was performed with the help of Ansys® software limiting attention to a liner elasticity with the maximum applied force F_{el} selected at the proportionality limit observed experimentally. Majority of FEM models provided smaller deflections compared to measurements except for the material set adopting Young's moduli from the compression test. The best fit was observed for the material data set obtained from homogenization. No predominant preference among individual geometries was found promoting the computational model based on reduced cross-section as sufficiently accurate.

KEYWORDS: GLT beam, three point bending test, fire test, effective residual cross-section.

1. INTRODUCTION

Glued laminated timber (GLT) enables wood to be used for more complex constructions with larger spans than used for common wood trusses. However, it also brings larger demands on its reliability. Probably, the most pronounced disadvantage of wood as a structural element is its combustibility. It must be taken into account in every design. The main task is a residual load bearing capacity of individual elements.

Eurocode 5 Part 1–2 [1] provides simplified methods to verify mechanical resistance based on a reduced cross-section or reduced properties. The reduced cross-section method introduces an effective cross-section with the same shape as the initial one assuming that the layer close to char line (d_0) has zero strength and stiffness, while the properties of the remaining material below this layer are assumed to be unchanged. Dimensions of an effective cross-section are the initial ones reduced by the effective charring depth:

$$d_{\mathrm{eff}} = d_{\mathrm{char},n} + k_0 d_0, \qquad (1)$$

where $d_{\mathrm{char},n}$ is the notional charring depth which accounts for corner rounding. The coefficient $k_0 = 1$ for unprotected surfaces and time longer than 20 min. The parameter $d_0 = 7$ mm represents zero strength and stiffness layer. Point out that d_0 could be even larger, in the range of 9.5 to 20.1 mm according to literature [2, 3]. Eurocode 5 also enables the application of advanced calculation methods (Annex B), usually based on thermal response model.

In this paper, we focused our attention on the behaviour of residual cross-section in three point bending. Comparison of three beam shapes was performed in finite element software Ansys® (Section 3), employing the results from three point bending tests (Subsection 2.2) and charring depth measurements (Subsection 2.1).

2. EXPERIMENTAL PART

The Experimental part of research is based on a fire test and supporting mechanical tests. The fire test setup and testing procedure are elaborated in [4, 5] and are briefly outlined here for the sake of completeness.

Altogether, sixteen GLT beams made of Norway spruce wood with dimensions $0.10 \times 0.32 \times 2.38$ m (Group 1; Samples 1–8) and $0.16 \times 0.32 \times 2.40$ m (Group 2; Samples 9–16) were tested, where all of them contained eight rows of lamellae connected vertically by plain joints and horizontally by finger joints with melamine-urea-formaldehyde glue. Prior to the fire test, all beams were subjected to a series of Pilodyn 6J indentation tests, briefly mentioned in Section 3. A horizontal experimental setup was prepared in a way to simulate the wooden ceiling. Each setup (i.e. fire test) contained two beams; one equipped with eleven K type thermocouples in various positions to provide the temperature distribution during the test whereas the second beam was primarily intended for three point bending test.

Two temperature settings were used; the first one corresponding to ČSN EN 1363-1 curve (Samples 1–4

(A). Four side burning showing measuring points for charring depths.

(B). Three side burning with depicted lamellae.

FIGURE 1. Cross-sections with four side burning showing measuring points for charring depths and three side burning with depicted lamellae - both rotated anticlockwise.

	L [mm]	w_{el} [mm]	F_{el} [kN]	h [mm]	b [mm]	d_{mean} [mm]	d_0 [mm]	d_{eff} [mm]	h_{eff} [mm]	b_{eff} [mm]	E_1 [GPa]
1	2280	4.97	6.47	320	100	30.95	7	37.95	244	24	11.99
3	2280	11.96	23.62	320	100	20.90	7	27.90	264	44	11.92
5	2280	9.45	24.07	320	100	17.86	7	24.86	270	50	11.55
7	2280	9.64	37.32	320	100	13.76	7	20.76	278	58	11.79
9	2300	7.28	69.33	320	160	17.42	7	24.42	271	111	11.85
11	2300	9.99	71.01	320	160	23.77	7	30.77	258	98	11.10
13	2300	8.88	92.09	320	160	9.76	7	16.76	286	126	12.03
15	2300	7.59	30.38	320	160	31.13	7	38.13	244	84	11.91

TABLE 1. Input data for computational model.

and 9–16) and the second one with the same initial stage up to 600 °C which was then set constant (Samples 5–8). After the required time (60 min, 40 min, 30 min, 20 min) the test was terminated, beams extinguished with water stream, mechanically cleaned from charcoal layer and let to dry at ambient temperature.

2.1. CHARRING DEPTH

Charring depth is defined as "*the distance between the outer surface of the original member and the position of the char line*", where "*the position of the char line should be taken as the position of the 300-degree isotherm*" [1]. In this paper we assumed the char line to be the line, where the wood colour is changed from its original tone, i.e. visible browning, due to measurement via image analysis.

Dried and cleaned beams were cut lengthwise into pieces (Group 1: 10 pieces, $20\,\mathrm{cm} - 8 \times 25\,\mathrm{cm} - 18\,\mathrm{cm}$; Group 2: 11 pieces, $12\,\mathrm{cm} - 9 \times 24\,\mathrm{cm} - 12\,\mathrm{cm}$). All sections were documented by a DSLR camera Canon EOS 600D held in hand, with an effort to eliminate image distortion as much as possible. The images were subsequently edited, scaled, and inserted into rectangle with original dimensions. The charring depths were measured along both sides of four innermost lamellae as the distance from sides to first non-white pixel, comprising 66 measuring points (80 mm from top and bottom, 5 mm in between), as depicted in Figure 1a. Four innermost lamellae were chosen to ensure comparability among all cuts, because both three side (Figure 1b) and four side (Figure 1a) burning occurred. The whole procedure is described in detail in [4].

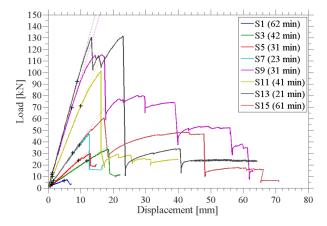The mean values of the measured charring depths for individual beams d_{mean} are listed in Table 1.

FIGURE 2. Load-displacement curves of the three point bending test.

2.2. THREE POINT BENDING TEST

Three point bending test belongs to commonly used experiments to determine the mechanical response of a structural element. Only odd-numbered dried and cleaned residual beams (i.e. after fire test) were tested in the displacement control regime with loading rate of $0.02\,\mathrm{mm\cdot s^{-1}}$. The load was applied on beam via steel plate or channel section plate, while the displacement of the midsection was continuously measured by a string potentiometer attached to the middle of the beam bottom edge. Each beam was supported by rollers on both ends and propped by wood blocks on both sides on each end to prevent tilting. More information could be found in [7].

Three quantities were recorded during the test: time, applied force, and maximum displacement in the midspan of the beam. The resulting load-displacement curves are plotted in Figure 2. Linear sections are

	E_y E_R [GPa]	E_z E_T [GPa]	E_x E_L [GPa]	G_{xz} G_{LT} [GPa]	G_{xy} G_{LR} [GPa]	G_{yz} G_{RT} [GPa]	ν_{yz} ν_{RT} [-]	ν_{xy} ν_{LR} [-]	ν_{xz} ν_{LT} [-]	
Iso 1			9.47					0.47		[6]
Iso 2			$E_1{}^b$					0.47		
Ortho 1[a]	1.30	1.92	9.47	1.70	1.25	0.42	0.28	0.47	0.47	[6]
Ortho 2	1.30	1.92	$E_1{}^b$	1.70	1.25	0.42	0.28	0.47	0.47	
Ortho 3	0.24	0.13	10.08	1.70	1.25	0.42	0.28	0.47	0.47	

[a] Mechanical properties of Norway spruce obtained by homogenization (MFA=28.24°).

[b] Average longitudinal Young's moduli measured by Pilodyn device before fire test stored in Table 1.

TABLE 2. Material input data for computational model.

marked by crosses. The force-displacement pairs corresponding to the upper cross (w_{el}, F_{el}), i.e. the proportionality limit, are summarized in Table 1 together with the beam span L, i.e. the distance between rollers.

3. Computational part

The main objective of this article is to show whether the simplified approach using the effective cross-section to determine the residual load bearing capacity of wood structural element is sufficient. Therefore, this section presents the comparison between finite element models employing the effective cross-section, which is considered rectangular and takes into account the charring depth and the zero strength and stiffness layer, with those reflecting the actual charring depth.

Besides the influence of the beam shape, five types of material input data were applied to demonstrate the impact of the selected material parameters.

All FEM simulations were carried out in the student version of the Ansys® software.

3.1. Material parameters

Five types of material input parameters were implemented: two considering isotropic behaviour and three assuming material orthotropy, see Table 2. All data sets are based on mechanical parameters of Norway spruce *Ortho 1* [6] computed by homogenization [8] for the microfibril angle (MFA) of 28.24°. The *Iso 1* assumes the longitudinal direction of *Ortho 1* only. The data sets *Iso 2* and *Ortho 2* are the same as *Iso 1* and *Ortho 1* except for longitudinal Young's modulus, which is replaced by the mean value of E_1 (Table 1) provided by the Pilodyn measurements prior to a fire test. The moduli E_1 [GPa] were computed as:

$$E_1 = 19.367 - 0.5641d, \qquad (2)$$

where d [mm] is the measured indentation depth [9]. The measurement is elaborately described in [7, 10].

The last data set *Ortho 3* employs mean Young's moduli in all three directions (E_R, E_T, and E_L) derived from the compression test. This test was performed on small blocks with dimensions of $30 \times 30 \times$

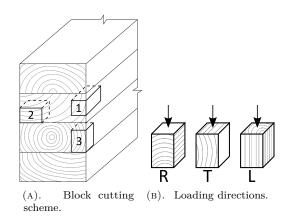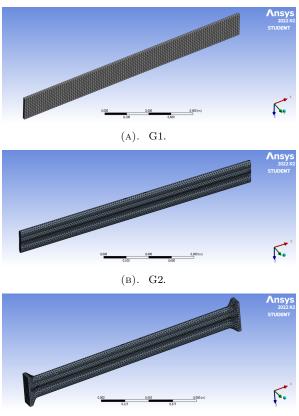
(A). Block cutting scheme.   (B). Loading directions.

FIGURE 3. Sample preparation for compression test.

40 mm cut from glued laminated timber beams not exposed to elevated temperatures (Figure 3a). Altogether, 17 blocks were loaded in three basic directions (Figure 3b) in displacement control regime using the MTS Aliance 30 kN electromechanical testing machine with loading rates of 2 mm · min^{-1} (L – longitudinal) and 8 mm · min^{-1} (R – radial, T – tangential). The moduli were determined from the initial slope of the stress-strain curves obtained from the measured load-displacement curves knowing the sample area and initial extensometer length.

3.2. Model definition

As was already mentioned, three types of beam geometries were modelled for the sake of comparison, see Figure 4, limiting attention to linear elasticity with material parameters summarized in the previous subsection.

Fifteen such FEM models were constructed for each beam, where the length of the modelled beam was set equal to the span between the supports denoted as L in Table 1. In the following, the actual residual cross-section of the midspan corresponds to the outline of the residual cross-section determined from the image of the segment cut in the middle of the beam length. The effective cross section employs Equation (1), while assuming the mean measured charring depth d_{mean} instead of

(A). G1.

(B). G2.

(C). G3.

FIGURE 4. Types of beam geometry (Sample 1) with depicted meshes.

the notional charring depth $d_{\text{char},n}$, and coefficient $k_0 = 1$, giving the effective cross-section dimensions as:

$$b_{\text{eff}} = b - 2d_{\text{eff}} = b - 2(d_{\text{mean}} + d_0), \qquad (3)$$
$$h_{\text{eff}} = h - 2d_{\text{eff}} = h - 2(d_{\text{mean}} + d_0), \qquad (4)$$

see also Figure 5.

Types of beam geometry:

- G1 = Effective rectangular cross-section with width b_{eff} and height h_{eff}, see Table 1, applied to the whole beam – constant cross-section (Figure 4a).

- G2 = Actual residual cross-section of the beam midspan applied to the whole beam – constant cross-section (Figure 4b).

- G3 = Actual residual cross-section of the beam midspan applied to the whole beam with pitched ends, both with 0.03 m initial rectangular cross-sections (b, h in Table 1) and 0.08 m of transition zone lengthwise – variable cross-section (Figure 4c).

The geometry was modelled as one solid element in SpaceClaim 2022 R2 and was imported to Ansys Workbench 2022 R2 employing the *Static structural analysis system*. The computation was performed considering a default setting, except for the element size and thus the mesh density. Limitations for the student license are 128K nodes/elements per model.
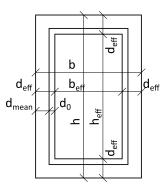

FIGURE 5. Effective cross-section.

Therefore, the element size had to be adjusted accordingly setting the initial size to 0.02 m. Larger elements (0.022 m) had to be adopted in the case of samples 9 and 13 when employing the actual residual cross-section both with and without pitched ends. The element types used in computations were SOLID186 (a higher order 3D 20-node structural solid element), SOLID187 (a high-order 3D 10-node tetrahedral structural solid element), and SURF154 (a 3D structural surface element).

Each beam was simply supported, with pinned support ($u_x = u_y = u_z = 0$) on the left end ($x = 0$) and roller support ($u_z = 0$) on the right end ($x = L$), both set as displacement boundary conditions at the bottom edges of beam ends. The force F_{el} (Table 1) was applied on the upper beam surface area over the entire width and 0.2 m lengthwise to reduce singularities. Note that the curved surface in the case of actual cross-section geometries brought some problems with the definition of the loading area on the upper surface of the beam (G2 and G3) and the bottom edge width (G2) for the introduction of supports, where in both cases borderlines were determined approximately.

4. RESULTS

The maximum deflection was determined approximately in the middle of the width at the midspan of the beam depending on the position of nodes (i.e. the value in the node closest to the required position was considered). The values closest to the deflection w_{el} in Table 1 (i.e. $\min |w_{\text{el}} - w_{\text{FEM}}|$) are highlighted by bold text in Tables 3, 4, and 5 for individual geometries and material parameters. The values with absolute difference less than 0.001 m from the measured values (i.e. $|w_{\text{el}} - w_{\text{FEM}}| < 0.001$) are highlighted as underlined text. According to the highlighted values, there seems to be no significant preference among individual geometries and among material parameters, separately. Although less accurate results seem to be predicted for *Iso 2* material data set considering isotropy with the longitudinal modulus measured by the Pilodyn device, while in the combination with G1 geometry it gives relatively good results. Probably the best approximation is provided by the data sets based

Beam	Fire dur. [min]	w_el [mm]	G1 (Effective cross-section) w_FEM [mm]					Nodes	Elements
			Iso 1	Iso 2	Ortho 1	Ortho 2	Ortho 3		
1	62.32	4.97	6.05	<u>4.78</u>	6.51	<u>5.30</u>	8.46	17323	2964
3	42.15	11.96	9.60	7.62	10.49	8.63	14.58	25355	4788
5	31.40	9.45	8.07	6.61	<u>8.87</u>	7.49	12.58	25355	4788
7	22.90	9.64	**9.92**	7.96	<u>10.97</u>	<u>9.13</u>	16.01	25355	4788
9	30.82	7.28	<u>10.61</u>	8.48	11.64	<u>9.63</u>	16.44	46461	9744
11	40.70	9.99	14.17	12.09	15.38	13.41	20.75	36888	7540
13	20.55	8.88	10.64	<u>8.38</u>	11.83	<u>9.71</u>	17.64	56968	12180
15	60.95	7.59	<u>8.31</u>	<u>6.61</u>	8.93	**<u>7.30</u>**	11.51	36888	7540

TABLE 3. Deflection w [mm] in the midspan computed by FEM model with geometry G1 – Effective cross-section (underlined text: $|w_\mathrm{el} - w_\mathrm{FEM}| < 0.001\,\mathrm{m}$; bold text: $\min(|w_\mathrm{el} - w_\mathrm{FEM}|)$ for each beam).

Beam	Fire dur. [min]	w_el [mm]	G2 (Actual cross-section) w_FEM [mm]					Nodes	Elements
			Iso 1	Iso 2	Ortho 1	Ortho 2	Ortho 3		
1	62.32	4.97	<u>4.74</u>	3.74	<u>5.04</u>	<u>4.09</u>	<u>5.83</u>	38553	22975
3	42.15	11.96	7.88	6.26	<u>8.61</u>	7.07	**11.23**	63479	40297
5	31.40	9.45	6.59	5.40	7.24	6.12	**<u>9.72</u>**	66795	43073
7	22.90	9.64	7.97	6.40	<u>8.80</u>	7.32	<u>11.63</u>	49566	10374
9	30.82	7.28	<u>6.57</u>	5.25	**7.39**	6.16	10.23	109639	74478
11	40.70	9.99	<u>10.15</u>	8.66	11.20	<u>9.79</u>	14.79	63772	13800
13	20.55	8.88	<u>7.87</u>	6.20	**8.88**	<u>7.32</u>	12.73	57628	12600
15	60.95	7.59	5.51	4.38	<u>6.10</u>	5.03	<u>8.46</u>	97053	65093

TABLE 4. Deflection w [mm] in the midspan computed by FEM model with geometry G2 – Actual cross-section (underlined text: $|w_\mathrm{el} - w_\mathrm{FEM}| < 0.001\,\mathrm{m}$; bold text: $\min(|w_\mathrm{el} - w_\mathrm{FEM}|)$ for each beam).

Beam	Fire dur. [min]	w_el [mm]	G3 (Actual cross-section with pitched ends) w_FEM [mm]					Nodes	Elements
			Iso 1	Iso 2	Ortho 1	Ortho 2	Ortho 3		
1	62.32	4.97	<u>4.73</u>	3.73	**4.96**	<u>4.00</u>	<u>5.86</u>	43840	26345
3	42.15	11.96	<u>7.84</u>	6.23	<u>8.42</u>	6.88	<u>11.12</u>	68074	43339
5	31.40	9.45	6.56	5.38	7.11	5.99	<u>9.80</u>	70451	45496
7	22.90	9.64	7.97	6.40	<u>8.74</u>	7.26	<u>12.52</u>	79277	52229
9	30.82	7.28	<u>6.61</u>	5.28	<u>7.39</u>	6.16	11.14	111654	75792
11	40.70	9.99	**<u>10.13</u>**	8.64	11.07	<u>9.67</u>	15.82	118967	80697
13	20.55	8.88	<u>7.87</u>	6.20	<u>8.88</u>	7.32	13.85	118919	81313
15	60.95	7.59	5.46	4.34	<u>5.90</u>	4.84	<u>7.92</u>	103695	69460

TABLE 5. Deflection w [mm] in the midspan computed by FEM model with geometry G3 – Actual cross-section with pitched ends (underlined text: $|w_\mathrm{el} - w_\mathrm{FEM}| < 0.001\,\mathrm{m}$; bold text: $\min(|w_\mathrm{el} - w_\mathrm{FEM}|)$ for each beam).

on homogenization *Iso 1* and *Ortho 1* in combination with geometries G2 and G3.

From highlighted numbers in Tables 4 and 5 it could be concluded that the geometries G2 and G3 are more or less comparable and there is no need to model pitched ends. However, the curved bottom ends in geometry G2 brought problems with the introduction of supports and caused non-symmetric vertical reactions. This was eliminated by considering straight edges used in G3 geometry with pitched ends.

Nonetheless, the simplest geometry G1, considering the rectangular cross-section only, does not deviate

from the accuracy point of view when compared to geometries G2 and G3. Therefore, it is reasonable to employ the most simple way in estimating the residual load bearing capacity based on the effective cross-section method.

By comparing deflections in Tables 3, 4, and 5, we observe that the majority of computed values w_FEM are lower than the measured value w_el being numerous in the case of data sets *Iso 2* and *Ortho 2* with longitudinal modulus measured by the Pilodyn device. This is reasonable, because the FEM models are usually stiffer compare to reality approaching the exact

solution from below with increasing mesh density.

An exception are the results obtained with material parameters *Ortho 3* data set showing predominantly higher values with some even twice as large as the measured ones, even though some were very close. This model thus appears too compliant.

5. CONCLUSIONS

This paper examined a suitability of the reduced cross-section method (G1) described in Eurocode 5 Part 1–2 [1] in the prediction of the behaviour of a beam subjected to fire. To that end, the results obtained experimentally from three-point bending tests were simulated numerically with the help of Ansys® finite element software. The results obtained from the application of the reduced cross-section method (G1) were also compared with the response provided by models assuming actual measured residual cross-section of burnt beams (G2 and G3). Apart from variable cross-section geometries, five types of material input parameters were implemented, recall Table 2.

All beams were modelled as simply supported (supports prescribed as displacement boundary conditions on the bottom edge of each end) with the force F_{el} (measured force at the proportionality limit) applied on the upper beam surface area. The linear elasticity was considered only. The maximum deflection was determined in the middle of the cross-section width in the midspan of the beam.

The numerically obtained deflections w_{FEM} are compared in Tables 3, 4, and 5 with the values w_{el} measured experimentally at the proportionality limit. Considering the values with the absolute difference less than $0.001\,\mathrm{m}$, we observe no prevailing preference among individual geometries or material parameters, separately. It could also be concluded that geometries G2 and G3 are more or less comparable. However, unlike G3 the curved edges of G2 resulted in non-symmetric vertical reactions. It is also evident that from the accuracy point of view the most simple geometry G1 is comparable to both more complex geometries G2 and G3 thus promoting the use of the reduced cross-section method in numerical simulations.

As for individual material settings, probably the best approximation gives the combination of *Iso 1* and *Ortho 1* data sets obtained by homogenization with the geometrical model G3. The effective cross-section based model G1 provided the best fit with *Iso 2* and *Ortho 2* data sets. The least accurate results were predicted by combining the G1 model with the *Ortho 3* data set. Remember that the use of *Ortho 3* resulted in much higher deflections compare to experiments suggesting an excessively large model compliance.

Nonetheless, there still might be some uncertainties introduced within the model definition such as the way of applying the force, definition of supports, or material input parameters limited to elasticity. From the model definitions point of view we expect a potential improvement by redistributing the force by a steel plate as used in experiments. Further advancement should arise from the application of a nonlinear constitutive model to be calibrated on the basis of a nonlinear part of the stress-strain diagram provided by compression tests. We aim to compare both isotropic and orthotropic plasticity models with isotropic hardening in our future studies.

LIST OF SYMBOLS

L Span between supports [mm]

w_{el} Max. displacement at the proportionality limit [mm]

F_{el} Maximum force at the proportionality limit [kN]

b, h Initial beam dimensions (width, height) [mm]

d_{mean} Mean measured charring depth [mm]

d_0 Zero strength and stiffness layer ($d_0 = 7\,\mathrm{mm}$ [1]) [mm]

$d_{eff} = d_{mean} + d_0$ Effective depth [mm]

b_{eff}, h_{eff} Effective cross-section dimensions (width, height) [mm]

E_1 Longitudinal Young's modulus determined by Pilodyn device [mm]

E Young's modulus [GPa]

G Shear modulus [GPa]

ν Poisson's ratio [–]

w_{FEM} Maximum elastic displacement from finite element analysis [mm]

R, T, L Radial, tangential and longitudinal direction

REFERENCES

[1] European Committee for Standardization. Eurocode 5: Design of timber structures – Part 1-2: General – Structural fire design, 2004.

[2] J. Schmid, A. Just, M. Klippel, M. Fragiacomo. The reduced cross-section method for evaluation of the fire resistance of timber members: Discussion and determination of the zero-strength layer. *Fire technology* **51**(6):1285–1309, 2015. https://doi.org/10.1007/s10694-014-0421-6

[3] D. Lange, L. Boström, J. Schmid, J. Albrektsson. The influence of parametric fire scenarios on structural timber performance and reliability. Tech. rep., SP Technical Research Institute of Sweden, 2014. ISBN 978-91-87461-78-1.

[4] L. Kucíková, T. Janda, J. Sýkora, et al. Experimental and numerical investigation of the response of GLT beams exposed to fire. *Construction and Building Materials* **299**:123846, 2021. https://doi.org/10.1016/j.conbuildmat.2021.123846

[5] L. Kucíková, T. Janda, M. Šejnoha, J. Sýkora. Experimental investigation of fire resistance of GLT beams. *International Journal of Computational*

Methods and Experimental Measurements **8**(2):99–110, 2020. `https://doi.org/10.2495/CMEM-V8-N2-99-110`

[6] L. Kucíková. *Micromechanical study of spruce wood.* Master's thesis, Czech Technical University in Prague, Faculty of Civil Engineering, Department of Mechanics, 2018. [2022-12-09]. `http://hdl.handle.net/10467/74309`

[7] L. Kucíková, M. Šejnoha, T. Janda, et al. Mechanical properties of spruce wood extracted from GLT beams loaded by fire. *Sustainability* **13**(10):5494, 2021. `https://doi.org/10.3390/su13105494`

[8] M. Šejnoha, J. Sýkora, J. Vorel, et al. Moisture induced strains in spruce from homogenization and transient moisture transport analysis. *Computers & Structures* **220**:114–130, 2019. `https://doi.org/10.1016/j.compstruc.2019.04.008`

[9] M. Šejnoha, T. Janda, L. Melzerová, et al. Modeling glulams in linear range with parameters updated using Bayesian inference. *Engineering Structures* **138**:293–307, 2017. `https://doi.org/10.1016/j.engstruct.2017.02.021`

[10] L. Kucíková, M. Šejnoha, T. Janda, et al. Evaluation of impact of elevated temperatures on young's modulus of GLT beams. In *Acta Polytechnica CTU Proceedings. NMM 2020 Nano & Macro Mechanics*, vol. 30, pp. 41–47. 2021. `https://doi.org/10.14311/APP.2021.30.0041`